Influence of KCl and HCl on a laser clad FeCrAl alloy: *In-Situ* SEM and controlled environment High temperature corrosion

L. Reddy[a], M. Sattari[b], C.J. Davis[c], P.H. Shipway[a], M. Halvarsson[b], T. Hussain[a,*]

[a] *Faculty of Engineering, University of Nottingham, Nottingham, NG7 2RD, UK*
[b] *Division of Materials Microstructure, Department of Physics, Chalmers university of Technology, Kemivägen 10, 41296, Gothenburg, Sweden*
[c] *Materials and Corrosion Team, Technology Centre, Uniper Technologies Limited, Ratcliffe on Soar, Nottingham, NG11 0EE, UK*

ABSTRACT

This study investigated the effects of HCl and KCl on a laser-clad FeCrAl coating at 450 °C in an *in-situ* ESEM followed by a furnace exposure. In all *in-situ* TEM cross-sections, three major phases were identified: an iron rich oxide, an iron-chromium mixed oxide and an aluminium enriched layer. HCl allowed chlorine based corrosion to occur which suggests interaction from its gas phase. EDX of the regions around KCl crystals showed a decrease in chromium which is an indication of chlorine selectively removing chromium. Moreover, the mass gain in HCl with KCl was significantly lower than that observed in air with KCl.

1. Introduction

As we transit to more sustainable power generation, there has been an increase in the uptake of biomass combustion as an alternative to conventional fossil fuels [1]. Using biomass in a conventional fossil fuel boiler comes with specific challenges such as a more aggressive combustion environment, leading to increased material loss from boiler components, and significant reductions in operational performance [2].

One of the techniques used to combat the aggressive high temperature corrosion environments within boilers is to use corrosion resistant materials. Many of these materials are expensive, and as such it is not economically feasible to replace conventional ferritic steels. In these situations, a surface engineering solution or a corrosion resistant coating can be applied. One such technique is laser cladding, where the feedstock material is fed into a meltpool on the surface of the substrate generated by a laser—as the meltpool is moved across the surface a coating is built up.

Currently, materials used in heat exchanger components are mainly ferritic steels, and the most commonly used coating materials for heat exchangers are corrosion resistant nickel based chromia forming alloys [3]—an alternative is iron-based alloys (FeCr, FeAl, FeCrAl, *etc.*) due to the lower cost and abundance of iron. The addition of small amounts of aluminium into the traditional FeCr alloys to form FeCrAl alloy has been shown to allow the formation of alumina at temperatures above

900 °C [4]. Also, a thin transient aluminium oxide layer will form at temperatures of 600 °C on a FeCrAl alloy; however, this is most likely non-protective [3]. The formation of stable alumina—which only forms at a suitably high temperature with critical level of aluminium reservoir—is beneficial as it forms dense, thermodynamically stable protective layers [5].

It is well established in the literature that chloride salts play a particularly important role in biomass induced fireside corrosion due to their high levels in many biomass feedstocks [6,7]. In contrast to coal combustion, where typical deposits contain alkali-iron tri-sulfates, and zinc and lead chlorides in boilers firing municipal solid waste, most biomass combustion deposits are dominated by potassium chloride [8]. Also, hydrogen chloride is the most common chlorine containing species in biomass flue gas [8]. It has been shown that combustion of feedstocks produces HCl [9]. This concentration is increased further by by-products from the formation of alkali chromates in the presence of alkali salts and water vapour [10]. The protective oxides which form on the surface of metals are typically dense, and prevent further diffusion of oxygen to the scale-metal interface. This pacifies the surface and prevents further oxidation. HCl is able to diffuse through this dense protective oxide towards the metal-scale interface. Once at this interface—where the partial pressure of oxygen is low—the hydrogen and chloride dissociate as metal chlorides, and become more energetically favourable. Once formed, the metal chlorides can diffuse back through

the protective scale towards the scale-gas interface. Here in the higher partial pressures of oxygen, the metal chlorides are oxidised, releasing the chlorine to diffuse back through the protective scale in the same cycle as the hydrogen chloride.

FeCrAl alloys offer an alternative to conventionally used low alloy steels. The addition of aluminium enables the formation of alumina, as well as chromia scales. These scales are dense and thermodynamically stable. The current research into the effects of KCl and HCl on FeCrAl alloys is focused on two main areas: short scale, and long scale exposures. In short scale tests, it has been shown that pre-formed alumina scales, formed at 900 °C for 1 h, provide protection against chlorine attack. Flaws in this protective alumina layer provide pathways for chlorine ingress and the eventual failure of the coating [10]. Without pre-oxidation, at 600 °C, only an aluminium enrichment was detected at the scale-coating interface, and potassium chloride was able to react with the FeCrAl alloy as well as O_2 and H_2O present in the corrosion environment to form potassium chromate [3,11]. The other area of research is at much longer time scales. Here the effects of chlorine are looked at in more complex environments and for much longer durations. It was reported that in the longer term tests, the concentration of chromium is likely to play a more beneficial role in corrosion protection [12]. At 800 °C in complex chlorine rich environments the level of aluminium became important as alumina provided protection and reduced metal loss [13].

For much of the previous work discussed above, *In-Situ* Environmental Scanning Electron Microscopy (*In-Situ* ESEM) was used. *In-Situ* ESEM offers opportunities to investigate the progression of corrosion as it occurs. ESEM chambers allow carful control of the gaseous environment, and this can be paired with real time imaging of the sample. The technique allows for high temperature corrosion tests to be imaged in real time. When looking at iron, *in-situ* measurements allowed for the structure of the initial iron oxides that grow on the surface to be investigated, providing insight into the initial mechanisms [14]. The initial heating conditions of a sample can play an important role in its oxidation mechanisms [15].

The existing literature investigated the performance of FeCrAl alloys at temperatures of 600 °C or higher, and often in a pre-oxidised state. This work investigated a laser clad FeCrAl alloy on stainless steel at 450 °C, a temperature matching the current operational temperatures of biomass fired boilers. Despite this being a relatively small temperature change, it moves the temperature well away from the melting point of KCl, ensuring that interactions in the solid phase were investigated. There is little work carried out in the literature looking at laser clad coatings, whose dilution and microstructure may influence the corrosion performance of the coating material. This study combined relatively short-term (1 h) controlled environment exposure in an *in-situ* ESEM chamber with longer term exposure (250 h) in a laboratory furnace in similar environment (as well as more complex environment). The purpose here was to develop an understanding from the onset of corrosion at few nanometres to section loss experienced at longer term exposure. The *in-situ* tests can provide valuable information on KCl-laser clad FeCrAl interactions that will allow us to redesign these coating microstructure for industrial use. In this work, the effects of potassium chloride crystals and hydrogen chloride gas on the formation of oxides and other corrosion products on a laser clad FeCrAl alloy was investigated.

2. Materials and methods

2.1. Materials

Commercially available feedstock wire Kanthal APMT™ (Sandvik Heating Technology AB, Sweden) with composition (C < 0.08, Al = 5.0, Si < 0.7, Cr = 21.0, Mn < 0.4, Fe = 69.8 and Mo = 3.0 all in wt.%) was laser clad onto a stainless steel 304 substrate (C < 0.08, Cr < 20, Mn < 2, Ni < 12, N < 0.1, P < 0.045, Si < 0.75,

S < 0.03 and Fe Bal. all in wt.%). A front fed wire feed setup was used to feed the 1.2 mm wire feedstock into the laser spot. A 2 KW ytterbium-doped fibre laser (IPG Photonics, Germany) with a 600 μm fibre was used to deposit the Kanthal APMT wire feedstock onto a 200 mm × 100 mm × 6 mm 304 stainless steel plate. A spot size of 4 mm was produced with a 20 mm defocus. A power of 1800 W was used with a bed traverse speed of 3.3 mm s^{-1} and a wire feed rate of 6.6 mm s^{-1}. Each successive pass of the laser deposited at a step distance of 2.618 mm producing a 40% overlap coating. These parameters were selected from previous work on optimising coatings for corrosion performance [16]. This section of coated substrate was cut into 10 mm × 10 mm sections using a silicon carbide precision cut off disc. The top surface of each of these sections was ground sequentially with silicon carbide grinding papers and finally to a diamond finish to 1 μm.

2.2. In-situ ESEM exposure

The samples were deposited with a saturated solution of KCl in water and industrial methylated spirit pipetted onto the surface. *In-situ* high temperature oxidation tests were carried out in an FEI Quanta 200 Field Emission Gun Environmental Scanning Electron Microscope (FEG ESEM) (Thermo Fisher Scientific, MA). The setup of the SEM is the same as that found in previous work [15]. The prepared samples were exposed in laboratory air inside the ESEM at 1 Torr for 1 h. All micrographs were taken with a 15 kV beam voltage, a spot size of 4 and a working distance of 10 mm in secondary electron mode. The samples were heated at 450 °C for the duration of the exposure using a furnace heated stage, with water cooling mounted within the ESEM chamber. This heated stage was attached to a temperature control unit. The temperature of the heated stage was calibrated suing the melting points of tin and zinc.

An FEI Versa 3D FIB SEM (Thermo Fisher Scientific, MA) was used to carry out the FIB milling in this work. Micrographs were taken in BSE with a beam voltage of 10 kV and a spot size of 4. The samples milled were those that has been exposed in the *in-situ* SEM exposures. The regions of interest were first deposited with a 25 μm × 2 μm layer of platinum to protect the surface. The gallium ion source was then used to mill a trench on either side of this region. A 30 kV ion beam was used for this. The resultant wall between the two trenches was then undercut, leaving it attached on one side. An omniprobe tip was then stuck to the surface using platinum before the final support was milled using the ion beam. That sample was removed ready for imaging in TEM.

In TEM, using the effects of tunnelling through an ultra-thin sample, spatial as well as structural and compositional information scan be gained. An FEI Titan 80–300 scanning transmission electron microscope (Thermo Fisher Scientific, MA) was used to obtain all of the TEM micrographs. Micrographs were taken using the high angle annular dark field (HAADF) detector. This allowed for atomic resolution with contrast directly related to atomic weight.

2.3. Lab scale furnace exposure

Two test environments were used to carry out the high temperature controlled environment corrosion tests. The first environment was a circulating air box furnace, the second was a synthetic biomass flue gas containing 500 ppm HCl, 5% O_2 and N_2 balance, performed in a horizontal tube furnace with an internal diameter of 70 mm. The stainless steel reactor used in the furnace was lined with high purity alumina. The prepared samples were placed in individual alumina crucibles. Exposures were conducted in both environments for 250 h at 450 °C, as well as for 1 h in air at 450 °C to match the *in-situ* ESEM exposure of the sample. Before exposure, the samples were degreased and cleaned using ultrasonic agitation in IMS (industrial methylated spirits). The samples were split evenly into two groups: one group had a saturated solution of KCl in water and IMS pipetted onto the surface, which was left to

Table 1
High Temperature tests for all samples reported in this study.

In-situ ESEM exposure (450 °C for 1 h)	
1	1 Torr air without any KCl
2	1 Torr air with KCl
Lab scale box furnace exposure (450 °C for 1 h)	
1.	1 atm air without KCl
2.	1 atm air with KCl
Controlled Environment exposure (500 ppm HCl, 5 % O_2 and N_2 balance, 450 °C for 250 h)	
1	1 bar without KCl
2	1 bar with KCl

evaporate, leaving individual KCl crystals. The second group did not have any deposit.

A summary of all the test conditions were provided in Table 1. The environments were chosen to provide a thorough understanding of the oxidation of FeCrAl alloy in 1 Torr air inside an ESEM, at 1 atm in a box furnace and at 1 bar in 500 ppm HCl 5% O_2 and N_2 balance. The purpose of these test conditions were to study how oxide scales grew in air and in HCl. The *in-situ* ESEM work was designed to provide useful information on the early stage of oxidation. KCl is the main corrosive compound in biomass boilers, and hence all these three tests were also conducted in presence of KCl. The temperature was kept constant in all tests.

X-Ray Diffraction (XRD) was carried out on the top surface of the sample to determine the phases present within it. The XRD was carried out on a D500 Diffractometer (Siemens AG, Germany) with a diffracted-beam monochromator and scintillation counter detector. The instrument was operated at 40 kV and 20 mA to generate Cu Kα radiation at a wavelength of 0.1540 nm. The XRD scans were performed in the range $30° ≤ 2θ ≤ 90°$ with a step size of 0.08° and a dwell time of 8 s. This was performed both pre and post exposure.

After surface characterisation, the samples were cut, ground and polished using the same process as for the initial surface preparation; however, non-aqueous lubricants were used to ensure chlorides were not removed. These sections were cold mounted to protect any deposit formed, and were analysed with Scanning Electron Microscope (SEM) and Energy-Dispersive X-ray (EDX).

Micrographs of the top surface of the coatings were taken on an S-3400 N SEM (Hitachi High Technologies, IL) in Hi-Vac mode with 20 kV beam voltage, a working distance of 10 mm and a spot size 4. An 80 mm² spectrometer (Oxford Instruments, UK) was used to take these measurements and the analysis software INCA (Oxford Instruments, UK) to draw elemental information—this was again performed pre and post exposure.

3. Results

3.1. In-situ ESEM exposure of APMT

3.1.1. Areas without any KCl

Fig. 1(A) shows the exposed top surface of the APMT coating, free from KCl, and the corresponding TEM cross-section in Fig. 1(B). A protective platinum layer (above point A) is visible on the top surface of the oxides. As oxygen has been excluded from the EDX measurements, all percentages represent weight percentage (Fig. 2). A dual layer oxide can be seen to have formed on the surface (points A–C). Fig. 2 shows the elemental distribution along the line shown in Fig. 1. Moving from point A inwards, the chromium increases, from a minimum value at A of 9.9% to a maximum of 43.1%, well above the bulk composition. This is matched by a decrease in iron concentration over the same distance from its maximum at A of 82.6% to a minimum of 43.9%. This region represents an iron oxide with a thickness of approximately 10 nm,

giving a total oxide thickness of 16 nm. In Fig. 2, a high concentration of aluminium can be seen at the oxide-coating interface, suggesting the presence of aluminium rich oxide. Beyond this region, across the boundary at B, there is a chromium depletion over a distance of approximately 6 nm. Here chromium concentration reaches 13.8%. This is again matched by a change in iron as its concentration raises back to 74.5% over the same region. As oxygen has been excluded from the EDX measurements, this transition region most probably represents the iron-chromium spinel. Moving inwards from point B, we see a small region in Fig. 2 below the boundary at point B, approximately 15 nm thick, where chromium returns to its nominal bulk value of between 21.6 ± 0.1%. Iron also returns to its bulk value over this region of 67.7 ± 0.1%.

3.1.2. Areas with KCl deposit

Fig. 3 shows the evolution of a potassium chloride crystal during heating at 450 °C over the course of 1 h in the *in-situ* ESEM setup. It can be seen that in the case of this crystal, the KCl is evaporated during the heating, beginning at around 30 min. Regions of corrosion product can be seen beginning to form around the edge of the crystal as the KCl is consumed, and become especially evident after 40 min when the remaining KCl crystal has completely evaporated. Cross-section of this evaporated crystal can be seen in Fig. 4. The dark layer marked by line A–B is a thin layer of oxide above the surface of the coating. This is shown to be more separated from the underlying coating than that of the sample taken far from the evaporated crystal shown in Fig. 1. From Fig. 5, it can be seen that a double-layered oxide has again formed, similar to that seen in the sample without KCl. In the outermost region, at point A, an iron oxide forms with the chromium concentration dropping to 8.3% and the iron content increasing to 83.6%. Moving inwards, towards the coating-oxide interface, most likely an iron-chromium spinel forms which is approximately 10–15 nm thick. This contains 46.6% chromium and 30.3% iron.

In the bulk material, there is a depletion of both iron and chromium close to the coating-oxide interface at B. In the approximately 4 nm before the boundary, iron is depleted to 61.0%. The chromium depletes to a lesser extent but over a greater distance, dropping to 14.9% over a distance of approximately 22 nm. The region between points B and C again represent the bulk material and have a composition of 68.4 ± 0.2% iron and 21.6 ± 0.2% chromium. Fig. 5 also shows an aluminium enrichment at the coating oxide interface where the concentration is 10.0% compared to its measured bulk value between 5.0% and 6.1%. Finally, the presence of the KCl crystal can be evidenced, in the peaking of chlorine and potassium in the iron-chromium spinel layer with concentrations of 10.0% and 3.3% respectively.

3.2. XRD phases

Fig. 6 shows XRD scans of the coatings exposed in air and HCl for varying times without the presence of KCl. The peaks in the as-clad APMT could not be indexed accurately; it closely matches a number of iron-chromium and iron-aluminium mixed phases (PDF 03-065-4664, PDF 00-045-1203 respectively) with peak positions at 44.4°, 64.6° and 81.7° and associated d-spacing of 2.04 Å, 1.44 Å and 1.18 Å respectively. As such it is suggested that this is an iron solid solution containing chromium and aluminium, as would be expected from APMT. After 1 h, there were no oxide peaks found within the detection limit of the XRD. After 250 h in both air and HCl, peaks can be identified matching the crystal structure of haematite and chromia. It can also be seen that the presence of HCl increases the intensity of these peaks. Aside from these peaks there are no other phases visible from the XRD scans and as such, any other phases present under these conditions are expected to be very thin.

Fig. 7 shows XRD scans of the coating exposed in air and HCl for varying times with KCl. As observed in the samples exposed without the presence of KCl (as was observed in Fig. 6), the same iron solid solution
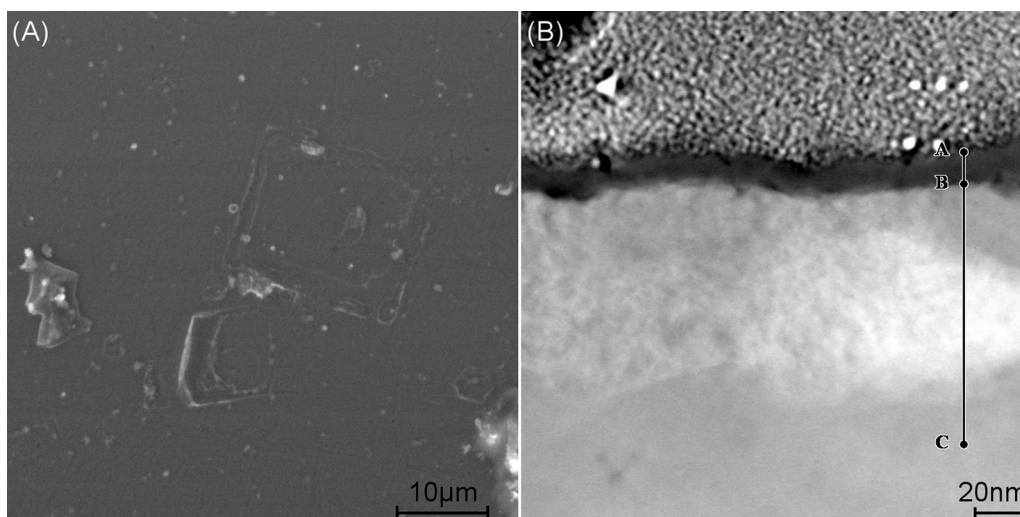
Fig. 1. (A) SE micrograph of top surface and (B) STEM-HAADF image of a FIB lift out cross section of the surface of the APMT coating exposed in laboratory air at 1 Torr at 450 °C. The section is taken through the site of a crystal shown in (A).
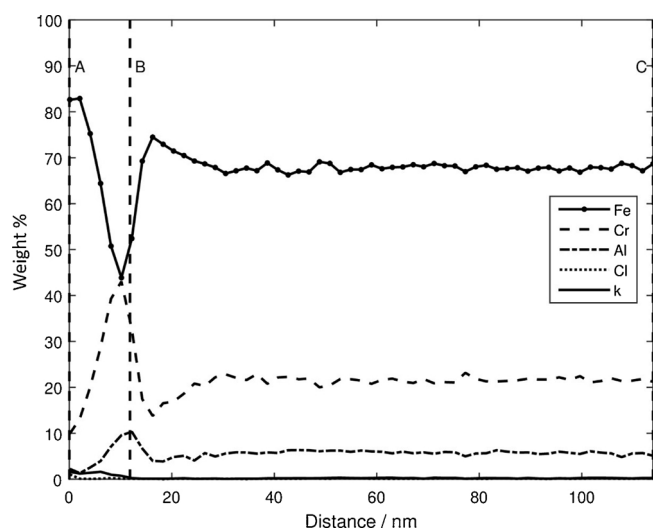
Fig. 2. Elemental distribution along the line shown in Fig. 1. There is an outer iron oxide which decreases as an iron-chromium oxide grows between points A and B. An aluminium rich region can also be seen at the interface denoted by the line B.

phase can be seen in all four scans. After 1 h in air in the presence of KCl, the β-hematite can be seen—this phase is also observed in sample without KCl. This is accompanied by α-hematite which is present in all samples when KCl is present. KCl is present in all of the samples and it is never fully consumed. After 250 h in the presence of HCl, the intensity of KCl in comparison to the other samples is lower, suggesting more of the KCl has been consumed. When the samples were exposed in air for 250 h, the coating peaks cannot be observed; this could be due to a thick layer of KCl covering the surface. There is an unindexed peak centred at a 2θ of 58°. This peak appears in all samples in the presence of KCl; however, a match could not be found.

3.3. Long term exposure of APMT in air

3.3.1. Samples without KCl deposit

After completing exposures in air for 1 h, long term exposures were carried out for 250 h. The top surface of the sample exposed without a KCl deposit can be seen in Fig. 8. Fig. 8(A) shows a low magnification image of the top surface. Much like the surface of the sample exposed for 1 h, there are very few features that can be seen on the surface of the

sample. The noticeable features that can be seen are shown in higher magnification in Fig. 8(B).

Table 2 provides information on the composition of these phases. Whilst point 1 is iron and chromium deficient compared to the substrate measured at point 2, it is enriched in manganese suggesting a manganese oxide on the surface. This was not picked up in the XRD shown in Fig. 6; however, these oxides are very small.

3.3.2. Samples with KCl deposit

When exposed for 250 h in the presence of KCl, the deposits which grow on the surface of the APMT (Fig. 9) are very different to those that are observed at shorter duration and without KCl. Fig. 9(A) shows a low magnification image of the surface. It can be seen that there is a continuous but variable covering over the entire surface of the coating. Higher magnification images show some of the complex phases present. Fig. 9(B) shows a thick, extruded tube like structure. These structures have cracks, and it can be seen from Table 3 to be rich in chlorine and chromium. The point 1 is the underlying iron oxide layer; however, it can be seen that this has been penetrated by chlorine in Table 3. The majority of the surface is covered with the oxide seen at point 2, another iron rich oxide again permeated with chlorine and potassium. Finally, point 3 shows the presence of potassium chromate.

3.4. Long term exposure of APMT with HCl

3.4.1. Samples without KCl deposit

After investigating the behaviour of the coating for different exposure lengths in air, a synthetic flue gas rich in HCl was used for a 250 h long test. The exposed samples surfaces can be seen in Fig. 10. At low magnification, as seen in Fig. 10(A), a fairly scattered deposit can be seen on the entire surface. Fig. 10(B) shows a typical structure that makes up the majority of the deposits seen on the surface. This deposit is covered by point 1 in Table 4. It is very thin so the results reflect mostly the underlying APMT coating; however, there is also chlorine present. Fig. 10(C) shows a plume like structure. These appear across the surface, and appears to originate from the pores. These pores are not observed in the as-clad coating, nor after any of the other condition except when HCl is present. Fig. 10(D) shows another chlorine rich deposit on the surface, showing that the gaseous HCl can interact with the surface.

3.4.2. Samples with KCl deposit

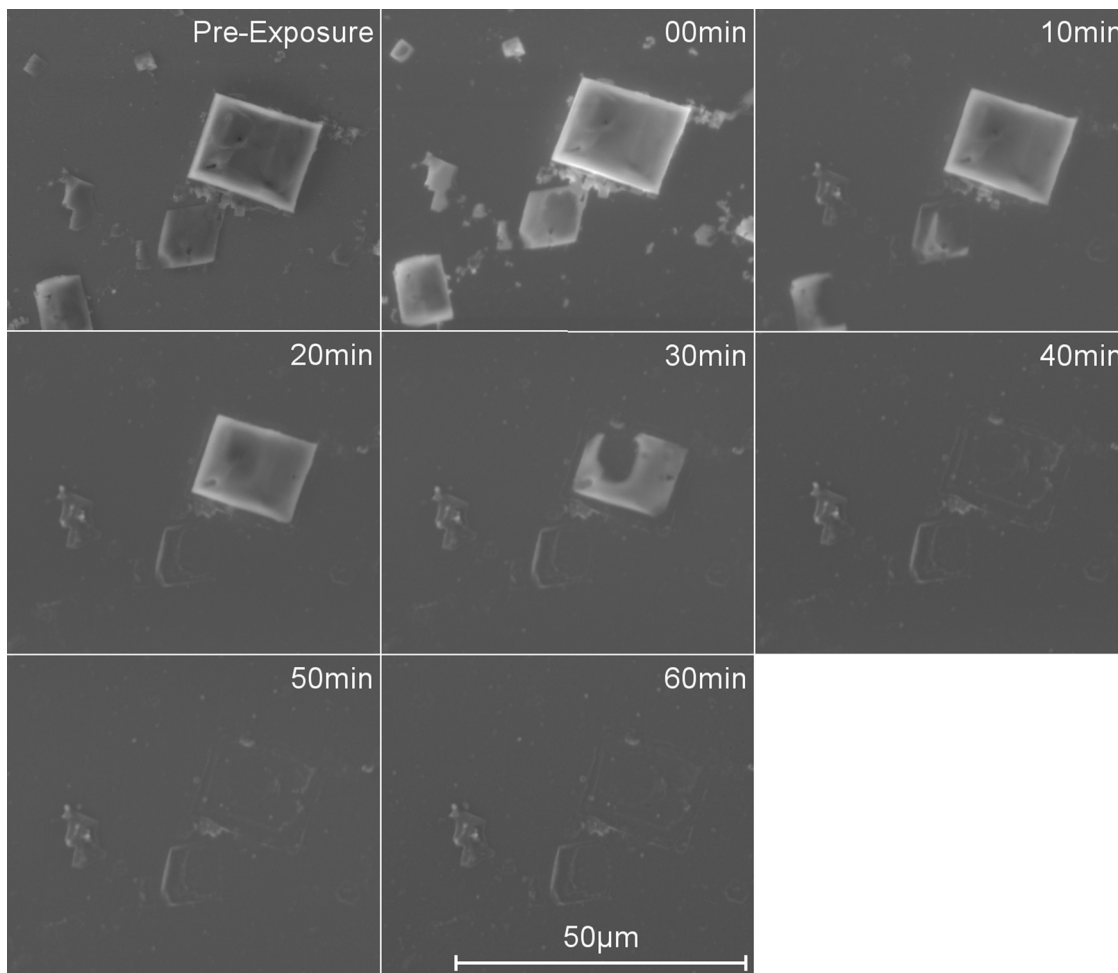The final sample was from the exposure condition where both HCl

Fig. 3. Time evolution of a KCl crystal on the surface of APMT coating exposed *in-situ* in laboratory air at 1 Torr at 450 °C over a 1 h timescale. The KCl crystal is consumed, however a thin deposit can be seen around its perimeter. All micrographs have the same scale.

gas and a KCl deposit were present. It can be seen in Fig. 11(A) that there is a complete covering of the sample with deposit. Fig. 11(B) shows the two different kind of components that are found on the surface: there is a thin, continuous oxide that covers the entire surface—this is very thin and as such, is difficult to detect with EDX—and the other feature on the surface is the chlorine rich tubes similar to those seen in Fig. 9(B). The elemental compositions of points: 1 & 2 in

Fig. 11(B) are shown in Table 5. Finally, the plume like structures originating from pores that were seen in Fig. 10(C) are longer and better defined under these conditions.

3.4.3. Mass change

Mass change was measured for all samples exposed in this study and these are shown in Fig. 12. All the samples showed mass gain in this
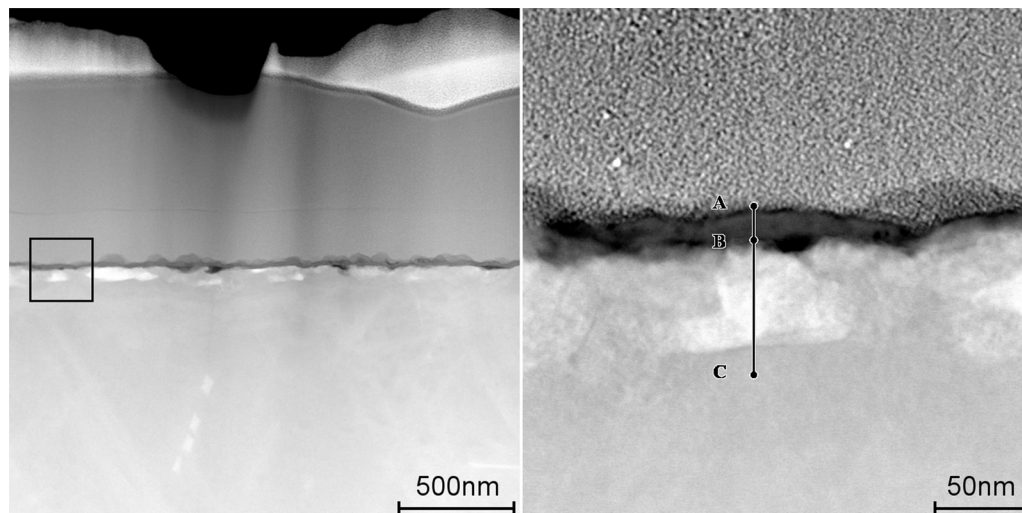

Fig. 4. STEM-HAADF images of a section of APMT coating exposed in laboratory air at 1 Torr at 450 °C. The section is taken close to the edge of a KCl crystal. In the left hand micrograph, platinum can be seen in the bright contrast and dark contrast region above the thin dark band of oxide. The micrograph on the right is a high magnification of the area marked by the box.
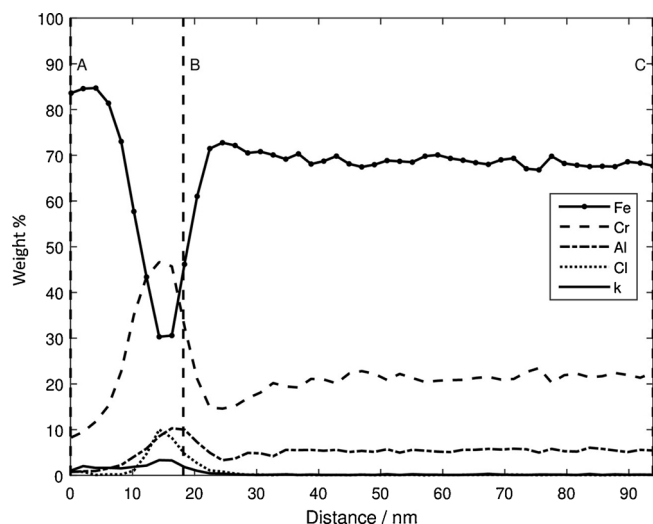
Fig. 5. Elemental distribution along the line shown in Fig. 4. A double layered oxide is seen in the dark region with an outer iron rich oxide, and an inner mixed chromium iron oxide. A rise in chlorine can be seen matching with the increase in chromium in the same region.
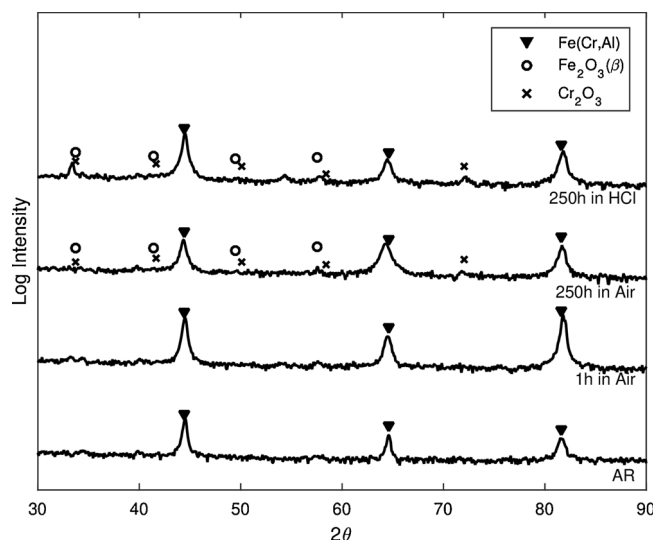

Fig. 6. XRD of APMT coating, as-coated and after 1 h and 250 h exposure at 450 °C in air and HCl.

study. The greatest mass gain arises when KCl is present in both air and HCl environments. The addition of HCl seems to have little effect without the presence of KCl; however, when KCl is present, it is observed to have a less damaging effect. Whilst HCl and KCl individually exhibit corrosive effects on the coatings, combined, the effect is reduced in comparison to KCl alone.

4. Discussion

4.1. Oxidation in air and HCl

In the TEM cross-sections of the clad exposed for 1 h in air without KCl there were three major phases identified at the coating-environment interface; an iron rich oxide, an iron-chromium mixed oxide and an aluminium enriched layer. There was a chromium depletion zone observed within the coating inward of the innermost mixed iron-chromium oxide layer. This outward movement of chromium is what causes the observed relative decrease in iron. In similar alloy systems such as stainless steel, the formation of mixed iron and chromium oxides is
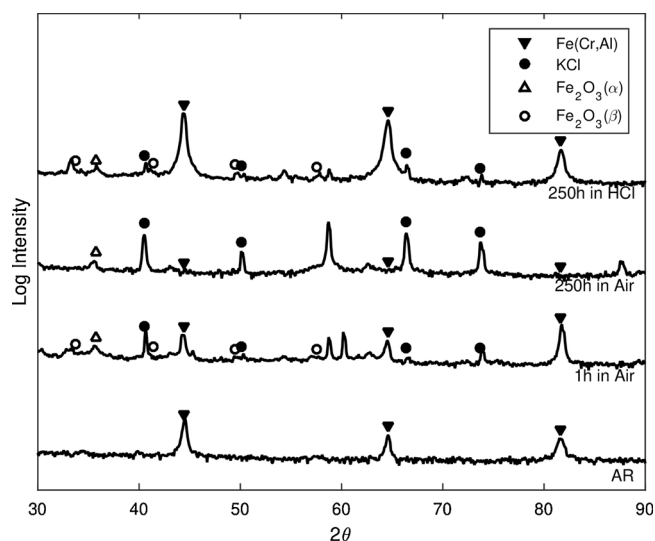

Fig. 7. XRD of APMT coating, as coated and after 1 h and 250 h exposure at 450 °C in air and HCl, with a KCl deposit.

expected and well documented in the literature [17]. A relatively thin region of aluminium enrichment is observed suggesting that the formation of the iron and chromium oxides is rapid. The phase diagram of the iron-chromium-oxygen system shows that a continuous series of solid solutions of Fe_2O_3 and Cr_2O_3 can form [17]. These can then form into spinels in solid solution with Fe_3O_4.

The final thing that can be noted from this *in-situ* exposure is the enrichment of aluminium at the initial coating-environment interface. The formation of aluminium oxide is expected to be very slow at temperatures of 450 °C. During early stages of oxidation, before the formation of thick corrosion products, aluminium based oxide can form; however, as fast growing iron and mixed oxide scales form, the oxygen partial pressure at the scale-substrate decreases, slowing the growth of aluminium based oxide further, preventing a thick layer from forming. This structure of a mixed oxide with aluminium enrichment at the coating-oxide interface is observed elsewhere in the literature under similar conditions in the alloy Kanthal AF [11].

Long term exposures were carried out for 250 h in four different environments: air without KCl, air with KCl, HCl without KCl, and HCl with KCl. In the simplest environment (air without KCl) the results observed were consistent with the short term exposures in that very little was observed on the surface within the limitations of SEM imaging. There is some evidence that manganese oxide formed on the surface. This is unexpected due to the minimal manganese in the coating (0.4 wt.%); however, this may be a region in which dilution of the substrate into the coating is high and as such the manganese concentration is higher in the coating.

Looking at the slightly more complex environment of HCl without KCl after 250 h, the features are similar to that in air exposure. The mass change of these two sets is very similar, initially suggesting that the presence of HCl does not affect corrosion. This is in line with different studies showing that at high partial pressure of oxygen and rather low HCl the influence is very small [23]. Like in an air environment, the observable reaction products are very small, and as such the similarities in mass change could be due to measurements of such small amounts of reaction product; despite this chlorine was detected on the surface of the sample under SEM analysis. This could be particularly important when looking at the plume like structures that have grown from pores in the sample (Fig. 10(C)). These features could represent the oxidation of metal chlorides that have formed at the lower oxygen partial pressures present inside a pore [18]. These plumes were extremely small but could signify the initiation of the reaction products found in exposures with KCl discussed later.
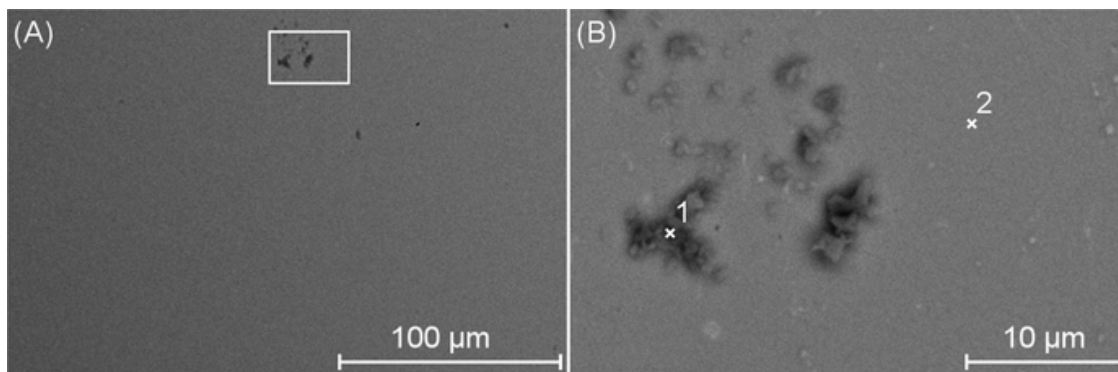
Fig. 8. BSE Micrograph of the oxides that have grown on the surface of APMT after exposure in air atmosphere for 250 h at 450 °C. In (A), isolated deposits of oxide can be seen on the surface. A high magnification of the area marked in (A) is shown in (B).

Table 2
Composition of Fig. 8 wt.%.

	Fe	Cr	Al	Si	Ni	Mo	Mn
1	57.3	18.1	4.2	3.4	2.9	2.9	11.3
2	69.0	21.0	3.2	0.4	3.3	3.2	

Table 3
Composition of Fig. 9 showing EDX results from points 1 to 3 in wt.%.

|	Fe	Cr	Al	Cl	Si	Ni	Mo	K
1	14.3	33.7	12.0	25.5		1.9	3.7	9
2	65.9	11.0	2.1	6.5	0.7	4.6	3.3	5.8
3	23.0	32.9	5.1	11.8	0.8	2.8	7.5	16.2

4.2. KCl deposit induced corrosion

Looking at the TEM cross sections (Fig. 4) of the APMT after 1 h *in-situ* exposure under KCl the same three major components are spotted as in the regions far from the KCl crystal: an iron rich oxide, an iron-chromium mixed oxide and an aluminium enriched layer. Additionally, a potassium chloride enrichment was observed at the original coating-environment interface. A chromium depletion zone was again observed within the coating after the innermost mixed oxide layer. When comparing the depth of this chromium depletion zone in the presence of KCl as opposed to areas far from the KCl crystals, it can be seen that both

the depth of the depletion zone, and the overall thickness of the reaction products are increased in the presence of the KCl. This increased thickness is especially true of the iron oxide that has grown outermost. It is well established that the presence of chlorine can inhibit the growth of chromium oxides, and as such could explain the increased thickness of the iron based outer oxide [3]. It can also be seen in Fig. 4(B) that there are voids that have formed along the oxide-coating interface—these voids appear as round dark spots between the oxide layer (A–B) and the coating. It is possible that these voids may have been formed by the removal of chromium in the form of chromium
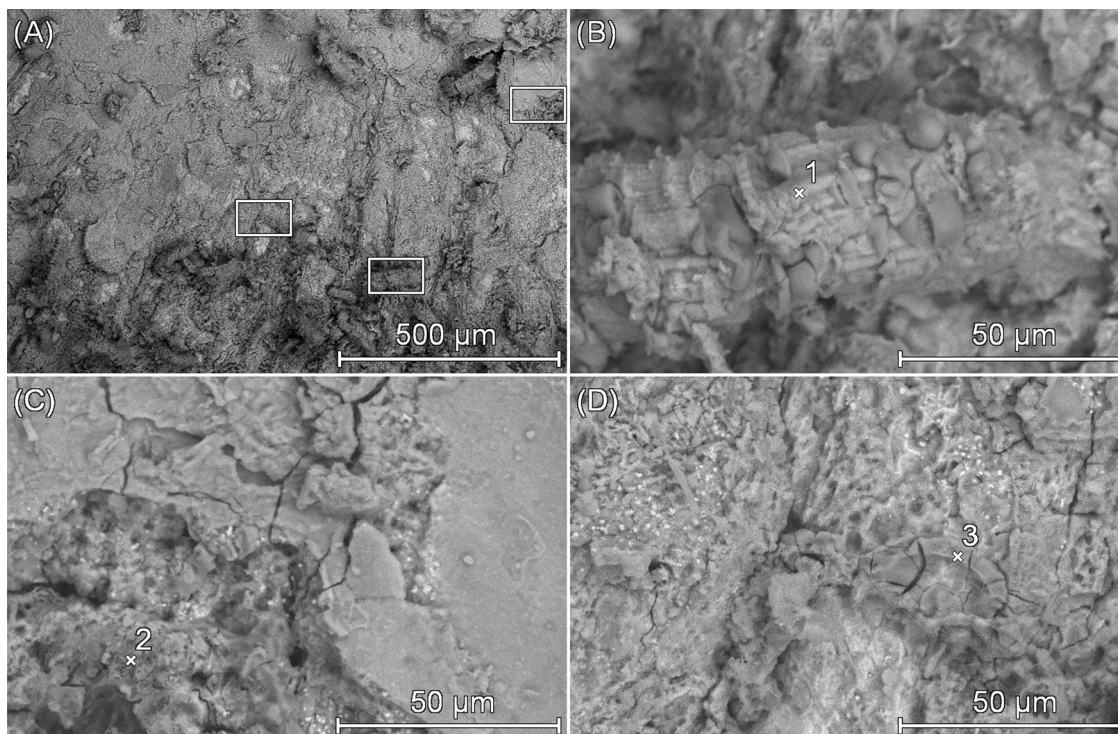
Fig. 9. BSE Micrograph of the oxides that have grown on the surface of APMT after exposure in air atmosphere for 250 h at 450 °C in the presence of KCl. In (A), the continuous deposit across the surface can be seen. A high magnification of the areas marked in (A) are shown in (B), (C) and (D).
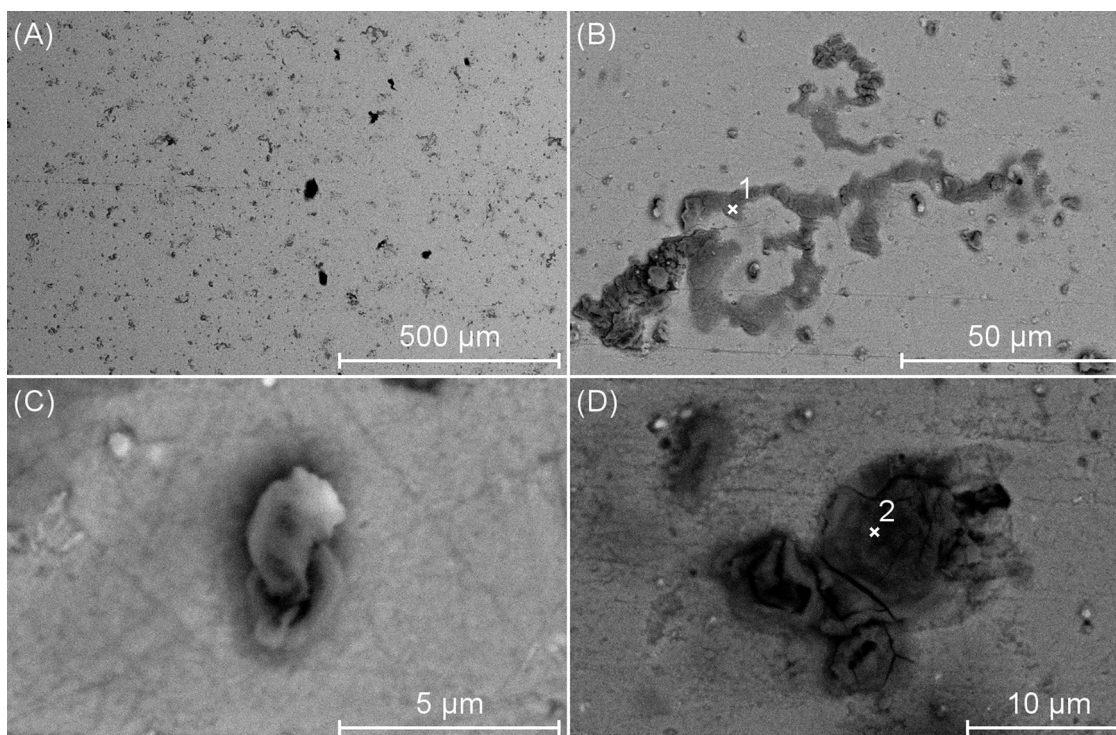
Fig. 10. BSE Micrograph of the oxides that have grown on the surface of APMT after exposure in HCl atmosphere for 250 h at 450 °C. A thin, non-continuous oxide can be seen across the surface in (A). One region of oxide that have grown on the surface of APMT can be seen in (B). A plume like structure is shown in (C). The other morphology of surface deposit not seen in (B) is shown in (D).

Table 4
Composition of Fig. 10 EDX points 1 and 2 in wt.%.

	Fe	Cr	Al	Cl	Si	Ni	Mo
1	64.6	20.7	6.8	2.8	0.9	2.6	1.7
2	63.3	22.0	6.6	2.5	1.0	3.0	1.5

Table 5
Composition of Fig. 11(B) EDX points 1 and 2 in wt.%.

	Fe	Cr	Al	Cl	Si	Ni	Mo	K
1	63.0	21.0	6.6	3.1	1.2	2.9	1.7	0.6
2	61.1	21.7	2.9	9.4	0.7	2.5	1.2	0.4

chlorides as has been seen in other work with iron-chromium-aluminium alloys [11]. This removal of chromium in the form of chlorides could also explain the increased depth of the chromium depletion zone despite the inhibited chromium oxide growth.

In the presence of KCl a much more extensive set of corrosion products are found on the APMT clad. These products are formed to a much greater extent than that which was observed without KCl. The formation of oxides exclusively at the sites of consumed KCl crystals is consistent with the results observed in the *in-situ* test, and supports the theory that KCl plays a role in increased mass gain in these samples.

EDX of the regions around former KCl crystals (point 2 in Fig. 9, EDX results in Table 3) show a decrease in chromium, when compared with other regions of the sample. This, paired with the expected increase in chlorine and potassium in these areas adds further credence to the theory that chlorine selectively removed chromium in a volatile phase, and is consistent with the results obtained from *in-situ* measurements. The increased rate of reaction product formation in the furnace test compared to that performed *in-situ* ESEM is not unexpected, and can be explained by the difference in oxygen partial pressure in each case, 4.46 kPa and 0.03 kPa respectively. The presence of potassium and
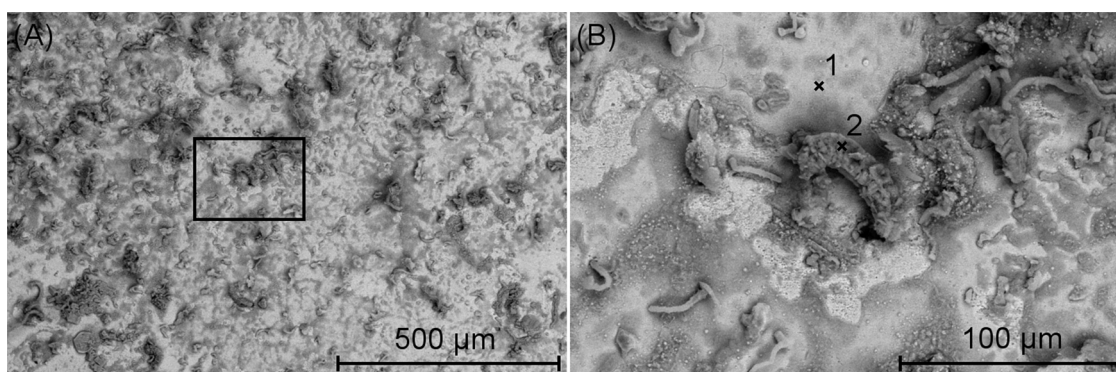
Fig. 11. BSE micrograph of the oxides that have grown on the surface of APMT after exposure in HCl atmosphere for 250 h at 450 °C with a KCl deposit. A more comprehensive, continuous oxide than without the presence of KCl can be seen across the surface in (A). (B) shows higher magnification images of the box.
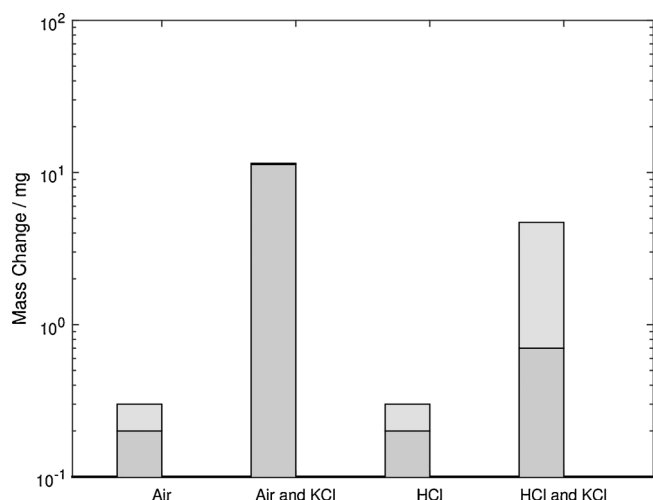
Fig. 12. Mass Change data for APMT coated samples in a range of environments and deposits. The light grey region represents the error in the measurement.

chlorine is also expected from the results of shorter exposures; however, it shows that over longer time scales it has neither been completely consumed nor evaporated, and is instead still present on the surface of the sample. The cause of the formation of the tube like structures which are not observed at shorter exposures *in-situ* ESEM is unexplained.

With the presence of HCl instead of air, the most notable result is the reduced mass gain in the coating with KCl as can be seen in Fig. 12. Whilst it can be seen that the mass gain is greater in both air and HCl when KCl is present, the mass gain in HCl with KCl is significantly lower than that observed in air with KCl. In an air environment, the only source of chlorine is from the dissociation of potassium and chlorine. The presence of HCl causes an increase in chlorine partial pressure which could slow the dissociation of potassium from chlorine and therefore cause the observed mass gain differences. It has been proposed that HCl can produce chlorine through the reaction shown in Eq. (1) [19].

$$4HCl + O_2 = 2Cl_2 + 2H_2O \tag{1}$$

This is consistent with the chlorine detected in EDX on the sample exposed in HCl without a KCl deposit, suggesting that the HCl gas is providing some chlorine to the surface.

4.3. Generalised mechanism of corrosion of APMT

At a much higher temperatures (above 900 °C), oxidation of aluminium to form alumina happens very briefly until the oxygen partial pressure drops low enough that chromium and iron start to diffuse outwards [17–23]. These form a Cr_2O_3 and Fe_3O_4 solid solution, which in time form a Fe-Cr spinel in solid solution with abundant Fe_3O_4. Although, the temperature in this work is relatively low, the fundamental mechanisms of formation of multi-layered oxides and spinel are still valid.

In this study, the formation of the plume like structures may be explained using the presence of HCl. It has been shown that Cl_2, rather than HCl itself is the main aggressive species [20]. This can be formed through Eq. (1). In low oxygen partial pressures, such as those found inside a pore, this chlorine gas can react with chromium or iron to form $FeCl_2$ and $CrCl_2$. Gaseous chlorine penetrates the oxide scale and reacts with the metal underneath, forming metal chlorines. These metal chlorides, as they diffuse towards the surface, are exposed to higher oxygen partial pressures where they undergo the following reaction according to Eq. (2) (M is Fe or Cr). The chlorine is available to move back into the coating, allowing corrosion to continue as part of the chlorine cycle [10,21–25].

$$4MCl_2 + 3O_2 = 4\,Cl_2 + 2M_2O_3 \tag{2}$$

When KCl is added to the system again, it gets more complex. Looking at KCl in an air environment, these mechanisms likely change again, which accounts for the vast differences in the corrosion products formed with and without KCl. As before, the initial stages of oxidation are the same, with the formation of Cr_2O_3. Once the Cr_2O_3 has formed, then it can react with the KCl and O_2 as through Eq. (3). This liberates chlorine, which is then available to diffuse back through the deposit towards the metal coating where it can form metal chlorides, beginning the chlorine cycle discussed above and shown in Eq. (2).

$$Cr_2O_3 + 4KCl + \frac{5}{2}O_2 = 2K_2CrO_4 + 2\,Cl_2 \tag{3}$$
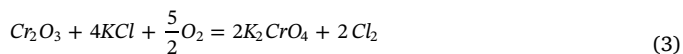
In the most complex environment, a combination of all of these processes are in action. Initially, corrosion will follow the mechanism described above in Eq. (3). The chlorine originating from the KCl will play a role in the chlorine cycle, moving metal ions to the surface in the form of metal chlorides. Under normal conditions in air, Eq. (2), these metal chlorides would be converted to metallic oxides at the surface, releasing chlorine to continue the cycle. This reaction will occur at a slower rate in the presence of HCl, due to the higher concentration of chlorine present at the surface already, formed from Eq. (1). The net result of this is that potassium chromate is still formed; however, chromium chloride is not converted to chromium oxide, causing chromium chloride deposits to form, and reducing the formation of chromium oxide. This reduction in the formation of chromium oxide accounts in part for the reduced mass gain observed when compared to APMT exposed in an air and KCl environment alone. The reduction in formation of chromium oxide through this mechanism is paired with the production of chromium chlorides. These chlorides are volatile, and can be removed at the gas oxide interface. This in turn contributes further to the reduced mass gain. It must be noted that this reduction in mass gain does not correlate to a reduction in corrosion rate.

This proposed mechanism is consistent with the results observed. In all cross-sections, an outer iron rich oxide is seen on top of an inner mixed spinel. The introduction of HCl shows the formation of a thicker oxide layer as well as evidence of potential potassium chromate forming from pores.

5. Conclusion

In this study, the corrosion mechanisms of the iron-chromium-aluminium Kanthal APMT laser clad were investigated. The corrosion performance was tested in *in-situ* ESEM, air and HCl rich environment for 1–250 h at 450 °C. All tests were carried out with and without the presence of KCl. The resulting corrosion products were analysed and the following conclusions can be drawn:

- Chlorine was found at the oxide-coating interface after only 1 h when KCl was present. This further supports the role that chlorine plays in corrosion of APMT.
- Aluminium is shown to migrate to the oxide-coating interface but no alumina was present in the coating at those exposure conditions.
- In the presence of a hydrogen chloride environment, chlorine can interact with the surface from the gas phase as well as from the potassium chloride.
- The presence of hydrogen chloride reduced the mass change of the samples deposited with KCl. This is proposed to occur due to the breakdown of hydrogen chloride and oxygen into water and gaseous chlorine, slowing the dissociation of potassium and chlorine and hence limiting the rate of oxidation.

Data availability

The raw data required to reproduce these findings cannot be shared

at this time due to technical or time limitations. The processed data required to reproduce these findings cannot be shared at this time due to technical or time limitations.

Acknowledgements

References

[1] J. Skea, P. Ekins, Making the Transition to a Secure and Low-carbon Energy System: Synthesis Report, in UKERC Energy 2050 Project, (2009), p. 25.

[2] R.W. Bryers, Fireside slagging, fouling, and high-temperature corrosion of heat-transfer surface due to impurities in steam-raising fuels, Prog. Energy Combust. Sci. 72 (1995) 29–120.

[3] N. Israelsson, et al., A microstructural and kinetic investigation of the KCl-Induced corrosion of an FeCrAl alloy at 600 °C, Oxid. Met. 84 (2015) 105–127.

[4] J. Engkvist, et al., Alumina scale formation on a powder metallurgical FeCrAl alloy (Kanthal APMT) at 900-1,100 °C in dry O_2 and in $O_2 + H_2O$, Oxid. Met. 73 (1-2) (2010) 233–253.

[5] G.J. Tatlock, et al., The effect of gas composition and contaminants on scale growth rates of FeCrAI alloys, Mater. Corros. 56 (12) (2005) 867–873.

[6] R. Saidur, et al., A review on biomass as a fuel for boilers, Renew. Sustain. Energy Rev. 15 (5) (2011) 2262–2289.

[7] B.M. Jenkins, et al., Combustion properties of biomass, Fuel Process. Technol. 54 (1-3) (1998) 17–46.

[8] H.P. Nielsen, et al., The implications of chlorine-associated corrosion on the operation of biomass-fired boilers, Prog. Energy Combust. Sci. 26 (3) (2000) 283–298.

[9] X. Ren, et al., Hydrogen chloride release from combustion of Corn Straw in a fixed bed, J. Energy Res. Technol. 140 (5) (2018).

[10] N. Israelsson, et al., Cyclic corrosion and chlorination of an FeCrAl alloy in the presence of KCl, Oxid. Met. 84 (3-4) (2015) 269–290.

[11] N. Israelsson, et al., KCl-Induced Corrosion of the FeCrAl Alloy Kanthal® AF at 600 °C and the Effect of H2O, Oxid. Met. 83 (1-2) (2014) 1–27.

[12] T. Hussain, et al., Fireside corrosion behavior of HVOF and plasma-sprayed coatings in advanced Coal/Biomass Co-fired power plants, J. Therm. Spray Technol. 22 (5) (2013) 797–807.

[13] T. Hussain, et al., Fireside corrosion degradation of HVOF thermal sprayed FeCrAl coatings at 700-800 °C, Surface and Coating Technol. 268 (2015) 165–172.

[14] B. Poter, et al., In-situ scanning electron microscopy and electron backscatter diffraction investigation on the oxidation of pure iron, Mater. High Temp. 22 (3-4) (2005) 185–193.

[15] T. Jonsson, et al., An ESEM in situ investigation of initial stages of the KCl induced high temperature corrosion of a Fe–2.25Cr–1Mo steel at 400 °C, Corros. Sci. 53 (2011) 2233–2246.

[16] L. Reddy, et al., Process parameter optimisation of laser clad iron based alloy: predictive models of deposition efficiency, porosity and dilution, Surface and Coating Technol. 349 (2018) 198–207.

[17] N. Birks, et al., Introduction to the High-Temperature Oxidation of Metals, 2nd ed., Cambridge University Press, New York, 2006.

[18] A. Zahs, et al., Chloridation and oxidation of iron, chromium, nickel and their alloys in chloridizing and oxidizing atmospheres at 400-700°C, Corros. Sci. 42 (2000) 1093–1122.

[19] M. Bai, et al., Experimental and thermodynamic investigations on the chlorine-induced corrosion of HVOF thermal sprayed NiAl coatings and 304 stainless steels at 700 °C, Corros. Sci. 135 (2018) 147–157.

[20] F.H. Stott, C.Y. Shih, The influence of HCl on the oxidation of iron at elevated temperatures, Mater. Corros. Und Korrosion 51 (5) (2000) 277–286.

[21] M. Montgomery, et al., Field test corrosion experiments in Denmark with biomass fuels Part 1: straw-firing, Mater. Corros. Und Korrosion 53 (2) (2002) 121–131.

[22] H.J. Grabke, et al., The effects of chlorides, hydrogen chloride, and sulfur dioxide in the oxidation of steels below deposits, Corros. Sci. 37 (7) (1995) 1023–1043.

[23] L. Krumm, M.C. Galetz, Impact of deposits and their morphology on the active corrosion of iron in chlorine- and sulfur-containing atmospheres in the tempearture range of 350-500 °C, Oxidation of Metal. 90 (2018) 265–381.

[24] N. Mortazavi, et al., In situ ESEM investigation of KCl-induced corrosion of a FeCrAl and model FeNiCrAl alloy in lab air at 450 °C, J. Electrochem. Soc. 162 (14) (2015) C744–C753.

[25] N. Israelsson, et al., KCl-induced corrosion of an FeCrAl alloy at 600°C in $O_2 + H_2O$ environemnt: the effect of pre-oxidation, Oxidation of Metal. 83 (2015) 29–53.